# The lawsonite-glaucophane blueschists of Elba Island (Italy)

## Journal Item

Journal Pre-proof

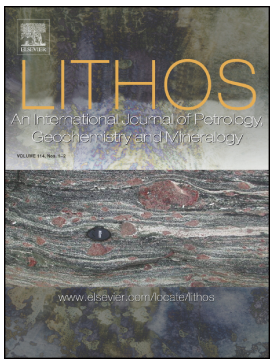


# The lawsonite-glaucophane blueschists of Elba Island (Italy)

Caterina Bianco, Gaston Godard, Alison Halton, Andrea Brogi, Domenico Liotta, Alfredo Caggianelli

PII: S0024-4937(19)30357-3

DOI: https://doi.org/10.1016/j.lithos.2019.105198

Reference: LITHOS 105198

To appear in: *LITHOS*

Received date: 1 April 2019

Revised date: 31 August 2019

Accepted date: 1 September 2019

Please cite this article as: C. Bianco, G. Godard, A. Halton, et al., The lawsonite-glaucophane blueschists of Elba Island (Italy), *LITHOS*(2019), https://doi.org/10.1016/j.lithos.2019.105198

# The lawsonite-glaucophane blueschists of Elba Island (Italy)

Caterina Bianco[1,*] caterina.bianco86@gmail.com; Gaston Godard[2]; Alison Halton[3]; Andrea Brogi[1,4]; Domenico Liotta[1,4]; Alfredo Caggianelli[1]

[1]University of Bari, Earth and Geo-Environmental Sciences, Via Orabona 4, 70125 Bari, Italy.

[2]Université de Paris, Institut de Physique du Globe de Paris, CNRS, F-75005 Paris, France.

[3]Faculty of Science, Technology, Engineering & Mathematics (STEM), The Open University, Walton Hall, Milton Keynes, MK7 6AA, United Kingdom.

[4]CNR-IGG, Institute of Geosciences and Earth Resources, Via G. Moruzzi 1, 56124 Pisa, Italy.

[*]Corresponding author.



## Abstract

Evidence for high-P blueschist-facies metamorphism was found in metabasites embedded in calcschists of Eastern Elba Island (Northern Apennines, Italy). Study of immobile trace elements (REEs and HFSEs) in the metabasites indicates an affinity with T- and E-MORBs, and they are interpreted as sill or dykes intruded in the western margin of the Adria continental plate. The minerals are heterogeneously distributed in the rock, constituting mafic and Ca-Al-rich microdomains inherited respectively from the magmatic pyroxene- and plagioclase-rich zones of the original doleritic rock. The peak pressure paragenesis consisted of lawsonite, aegirine-omphacite, glaucophane and chlorite. Former rhombic prism of lawsonite has been replaced by pseudomorphic clinozoisite (0.1 mm in size) with inclusions of Ms ± Ab ± Qz. The inclusions are preferentially oriented parallel to one of the diagonals of the basal rhombic sections, indicating that the two diagonals were not crystallographically equivalent. This implies that the protocrystals were orthorhombic prisms with {110} faces, which is the case of lawsonite. The different compositions shown by white mica and epidote in the pseudomorphs (muscovite and $Fe^{3+}$-poor clinozoisite) and in the matrix (phengite and $Fe^{3+}$-rich epidote) also suggest the former presence of Mg- and Fe-poor lawsonite in these rocks. Thermodynamic modelling, using the THERMOCALC software and dataset, suggests that metabasites experienced a clockwise P-T path from the lawsonite-blueschist to epidote-blueschist subfacies,

down to greenschist facies. The estimated peak pressure conditions are P ≥ 1.6 GPa and 450 < T < 500°C. Glaucophane grew mainly during the lawsonite-to-epidote transition and is dated at 19.8 ± 1.4 Ma by the $^{40}Ar/^{39}Ar$ method. This evolution is interpreted in terms: (i) intrusion of basic magmas in carbonatic and pelitic sediments (post-late Cretaceous, pre-Oligocene), (ii) subduction (Oligocene), (iii) collision (early Miocene: 19.8 ± 1.4 Ma), (iv) exhumation and granite intrusion (middle-late Miocene), favored by extensional tectonics. We underline that the eastern part of Elba Island belongs to a blueschist-facies belt that extends from Gorgona Island, in the northwest, to Argentario and Giglio Island in the southeast, so many of the conclusions of this study can be extended to the whole of this belt.

**Keywords**

HP-LT metamorphism, blueschist facies, Northern Apennines, Elba Island, P-T pseudosection, $^{40}Ar/^{39}Ar$ geochronology.

## 1. Introduction

In the Northern Tyrrhenian Sea (Fig. 1), from Corsica to Tuscany, high-pressure (HP) and low-temperature (LT) metamorphic conditions are widely recorded by metasediments and metabasites (e.g. Jolivet et al., 1998; Rossetti et al., 2002; Vignaroli et al., 2009). According to several authors (Carmignani et al., 1994; Rossetti et al., 2015 and references therein), the HP-LT events in the Tuscan archipelago and Tuscany (Fig. 1a) are related to the subduction and subsequent thickening of the Adria crust during the build-up of the Northern Apennines orogen, subsequently dismantled by extensional tectonics, active since early-middle Miocene (Brogi and Liotta, 2008; Molli, 2008; Barchi, 2010 and references therein).

From Corsica to Tuscany, peak pressures and metamorphic ages (Fig. 1) tend to decrease eastwards, from 2.2 to ~1 GPa (Rossetti et al., 2015 with reference therein) and from Palaeocene-Eocene to early Miocene (Brunet et al., 2000) during the westward formation of the Apennine orogenic tectonic pile (Molli, 2008; Brunet et al., 2000). In the Tuscan archipelago, the most common blueschist-facies index minerals are the carpholite-chloritoid pair and phengite in the metasediments, and glaucophane, lawsonite and jadeite-rich pyroxene in the metabasites, yielding estimated P-T values ranging between 0.6 and 1.5 GPa at 275–450°C (Fig. 1a).

Although structurally close to the Adria-Europe suture zone, Elba Island has been considered as a sector of the orogeny mostly affected by low-P (LP) metamorphism (Fig. 1). However, evidence for blueschist-facies HP-LT metamorphism has been found near Rio Marina (eastern Elba) in metasediments (Pandeli et al., 2001) and metabasites embedded in calcschists (Bianco et al., 2015). Achiardi (1896) also described so-called eclogites in central Elba, but these are actually rodingites embedded within serpentinite. Nevertheless, many uncertainties still concern the palaeogeographic pertinence of the tectonic unit hosting the HP-LT calcschists and metabasites: this tectonic unit has been attributed to the Adria continental margin (Keller and Pialli, 1990; Bianco et al., 2015) as well as to the Ligurian-Piedmont Ocean (Duranti et al., 1992; Pertusati et al., 1993; Pandeli et al., 2001), thus framing the HP-conditions to continental or oceanic subduction, respectively.

This study is focused on the metabasites discovered near Rio Marina, since the hosting calcschists, affected by late metasomatism and retrogression, appears less suitable for inferring the metamorphic evolution. The aim of this article is (i) to describe the HP-LT metabasites, (ii) to reconstruct their P-T history by thermodynamic modelling, (iii) to date this HP-LT metamorphism, (iv) to define which paleogeographic domain was involved in subduction-zone metamorphism, and (v) to better frame the Elba Island in the collisional evolution of the Northern Apennines. In order to reach these purposes, field mapping, mineralogical and petrological studies were combined with P-T pseudosection modelling and $^{40}$Ar-$^{39}$Ar datings.

## 2. Geological setting

### *2.1. Northern Apennines*

The Northern Apennines are the result of convergence and collision between the Adria microplate and the Sardinian-Corsican massif (Cretaceous-early Miocene), producing the eastward stacking of oceanic and continental tectonic units (e.g. Boccaletti et al., 1971; Molli, 2008), which experienced blueschist- to greenschist-facies metamorphism (Fig. 1; e.g. Gillet and Goffé, 1988; Carmignani et al., 1994; Giorgetti et al., 1998; Jolivet et al., 1998; Brunet et al., 2000; Rossetti et al., 2002; Molli, 2008; Vignaroli et al., 2009; Brogi and Giorgetti, 2012). In particular, metamorphic units in southern Tuscany experienced P-T conditions of 0.6–1.4 GPa and 350–450°C for the metasediments, and 0.7–0.8 GPa and 340–350°C for metabasites

(Kligfield et al., 1986; Giorgetti et al., 1998; Brogi and Giorgetti, 2012). Similarly, the metasediments of the Tuscan archipelago (Gorgona, Elba and Giglio islands) and Argentario Promontory have equilibrated at 1.0–1.5 GPa and T ≤ 350°C (Theye et al., 1997; Rossetti et al., 1999; Elter and Pandeli, 2002) while metabasites were formed at 0.6–1.2 GPa and 330–450°C (Fig. 1a; Bianco et al., 2015 and references therein). Since the early-middle Miocene, extensional tectonics (Fig. 1), migrating eastwards, affected the inner part of Northern Apennines (Carmignani et al., 1994; Molli, 2008; Barchi, 2010; Rossetti et al., 2015) and gave rise to exhumation of deeper units (Carmignani et al., 2004; Brogi, 2008; Molli, 2008), development of tectonic depressions in which marine to continental sediments deposited (Martini and Sagri, 1993) and widespread magmatism (Dini et al., 2002). The clearest evidence of this extensional process is the opening of the Tyrrhenian basin (Fig. 1).

This general framework has been recognized on Elba Island (i.e. Bortolotti et al., 2001), where seven main tectonic units (Bianco et al., 2015), belonging to continental or oceanic crustal environments (Bortolotti et al., 2001), have been described (Figs. 2 and 3). The stacking of oceanic and continental tectonic units, as well as their duplication by post-stacking out-of-sequence thrusts (Keller and Pialli, 1990; Pertusati et al., 1993), can be related to the ongoing compression during the convergence between Adria and Sardinia-Corsica. During the Miocene, extensional tectonics produced crustal detachments (Fig. 2), coeval and subsequent to the emplacement of the Monte Capanne (in western Elba; ~7.0 Ma: Westerman et al., 2004) and Porto Azzurro (in the eastern Elba; ~6 Ma: Maineri et al., 2003; Gagnevin et al., 2011) plutons, favoring the uplift and exhumation of both the plutons and their host rocks (Liotta et al., 2015, Zucchi et al., 2017 and references therein). Magma emplacement and cooling produced thermo-metamorphic aureoles, with LP mineral assemblages, overprinting older metamorphic paragenesis related to the collisional event (e.g. Duranti et al., 1992; Pertusati et al., 1993; Caggianelli et al., 2018).

### *2.2. The succession hosting the metabasites*

Blueschist-facies metabasites bodies, up to 1.5 m thick and 2 m long, have been found nearby Rio Marina (eastern Elba). These bodies are hosted by calcschists forming the basal part of the Continental Unit 2 defined by Bianco et al. (2015) (Fig. 3b; “Phy” in Fig. 4; Porticciolo subunit in Pandeli et al., 2001). This basal part is about 40 m thick and consists of calcschists and marbles (c in Fig. 3b), with cm-thick layers of

gray-green phyllites (Calcschists lithofacies in Bortolotti et al., 2015), where the studied metabasites lenses with HP metamorphic assemblage were recognized (Bianco et al., 2015; d in Fig. 3b). The upper 20 m include massive black phyllite passing to dark grey marble and calcschists, often interspersed with black to green phyllite.

The middle-upper part of the succession (i.e. Acquadolce Fm in Jacobs et al., 2018) is dominantly characterized by phyllite (b in Fig. 3b), and metasandstone and metasilstone up to 20 m thick (a in Fig. 3b). Minor cm- to dm-thick metasandstone levels occur as precursor in the underlying phyllite (b in Fig. 3b). Detrital zircon from the metasandstone levels has recently been studied by Jacobs et al. (2018), who interpreted it as derived from the volcanic arc, active during subduction and deposited in the foredeep of the Apennine orogen. Zircon dating by LA-ICP-MS and SHRIMP yielded a most populated age at 31.6 ± 0.5 Ma (Jacobs et al., 2018). The upper part of this succession, about 200 m in thickness, is interrupted by the tectonic contact with the Oceanic tectonic Unit 1 (Figs. 2 and 3b). Locally, the Continental tectonic Unit 2 has been affected by metasomatism that produced discontinuous bodies of hedenbergite-ilvaite-epidote skarn (Sk in Fig. 4).

## 3. Material and methods

Four representative metabasite samples (RMT3A, RMT4A, RMT7A and RMT19) were collected at the Rio Marina harbour (Figs. 2, 4-5), at the foot of the tower (N42°48’54.9”–E10°25’53.3”). These four samples belong to the same metabasite body, the maximum distance separating them being about 50 cm. Petrographic studies and bulk rock analyses were carried out for all samples. RMT3A was chosen for the P-T pseudosection modelling, being the most informative in terms of microstructures, while RMT7A was selected for dating, containing, optically, the most compositionally homogenous glaucophane. The RMT3A and RMT7A samples display very similar bulk rock composition with only slight variations in the decimals (Tab.1), so that the conclusions of the pseudosection modelling of RMT3A can be extended to RMT7A.

The analyses of the major elements were carried out on the four studied samples at the University of Bari, using Panalytical AXIOS-Advanced spectroscopy with X-ray tube SST-mAX (Super Sharp end-window Tube). Trace element analyses were performed on the same samples by ICP-MS at Actlabs® laboratories, in Canada. To reveal the microstructural relationships between minerals, backscattered electron (BSE) images and X-ray chemical element maps were obtained using a ZEISS Supra 55 VP scanning electron microscope

at *Ecce Terra* laboratory (Université Pierre-et-Marie-Curie, Paris, France), then processed with ENVI® software. Electron microprobe analyses were carried out using a Cameca SX-100 electron microprobe at *Camparis* laboratory in Paris, the analytical conditions were 10 nA beam current and 15 kV acceleration voltage. $^{40}Ar/^{39}Ar$ dating analysis was performed on glaucophane mineral separates at the Open University (UK), using step heating, with a MAP215-50 mass spectrometer and 1059 nm CSI fibre laser. Finally, to unravel the evolution of the metamorphic conditions, a P-T pseudosection was modelled by considering the composition of the RMT3A sample and using the THERMOCALC software (Powell and Holland, 1988; version 3.33 updated in June 2011) and the updated ds55 version of the thermodynamic dataset of Holland and Powell (2011). Mineral abbreviations are after Whitney and Evans (2010).

## 4. Petrography

The study metabasites belong to the basal part of the Continental Unit 2 (Figs. 2, 4-5). Here, marble and calcschists contain several segmented and isolated bodies of metabasites, from a few cm (Fig. 5b-c) to about 2 m long (Fig. 5d), wrapped by the main schistosity (i.e. the one observable at the outcrop scale and determining the main structural setting), gently SW/NW-dipping (stereogram in Fig. 5a). In the calcschists, this schistosity is locally deformed by tight, isoclinal folds (Fig. 5e), with ~300°/30° plunging hinge lines (Fig. 5e). A NW-SE-striking stretching lineation is clearly underlined by calcite and quartz elongation (Bianco et al., 2015). At microscale, the intense deformation of the calcschistsis also highlighted by widespread flattening and core-and-mantle microstructures (Fig. 6a-b), affecting both calcite and quartz, thus indicating progressive recrystallization processes. The mineral assemblage, oriented along the main schistosity, consists of Cal + Dol + Qz + Bt + Ph+ Chl ± Ti-Fe oxides ± Ab ± Ap ± Ep, as already reported in Bianco et al. (2015). Aragonite has not been reported.

The general mineral assemblage of the metabasite samples includes Gln + Cpx + Ep + Chl + Ab + Ms ± An ± Act ± Cal ± Qz ± Ttn ± Rt ± Ap ± Mag and it is indicative of former equilibration in the blueschist facies (Gln+Cpx+Ep) and later retrogression in the greenschist facies (Bianco et al., 2015). These rocks are fine-grained and display a mylonitic fabric characterized by clinopyroxene porphyroclasts dispersed in a matrix composed mainly of Ep + Gln + Chl + Ab + Ttn (Fig. 6c–f). Most of the glaucophane and minor actinolite are syn-kinematic, as they concentrate in the strain shadows of pyroxene porphyroclasts, wrapping

and forming stretched coronas around these (Fig. 6c, d). The rock exhibits strong heterogeneity, inherited in part from the magmatic protolith, with three main types of compositional microdomains:

(a) Mafic microdomains consist mainly of clinopyroxene porphyroclasts (Fig. 6c), a few millimetres across, which can be derived from magmatic pyroxene crystals. They are stretched and fractured, with glaucophane and chlorite filling the voids resulting from their parting (Fig. 7e, f). These porphyroclasts have been partially to completely replaced by fine-grained symplectites composed of Di + Qz + Chl ± Ab ± Ttn (Fig. 7).

(b) The Ca- and Al-rich microdomains of the matrix are mainly composed of epidote, calcite, titanite, glaucophane, micas, actinolite and albite (Fig. 7a-f). Epidote forms subhedral mm-sized grains, in which the BSE images commonly reveal chemical zoning mainly related to variations in the $Fe^{3+}$ content. RMT3A sample shows epidote single crystals containing inclusions of titanite, apatite, euhedral glaucophane with clearly recognizable basal sections (Figs. 6g, 8a-d), and especially poly-mineral inclusions of about 100 µm in size, which display regular prismatic or rhombic forms and consist of Czo + Ms ± Ab ± Qz ± Cal (Fig. 8). In other samples, these prismatic clinozoisite-bearing aggregates are embedded in chlorite and show only a thin epidote overgrowth (Fig. 7d, bottom). Because of their prismatic shapes, they are considered pseudomorphs after lawsonite, as later explained. Albite is common in the matrix and, in a few samples, anorthite is also present in the form of tiny crystals (Fig. 6e). Ilmenite, titanite, phengite, apatite and rutile, locally included in titanite crystals (Fig. 6f), are common accessory minerals of the matrix.

(c) Glaucophane, as well as minor actinolite, is well developed in the strain shadows of pyroxene porphyroclasts (Figs. 6c, 7a-b), and often wraps around them, forming very irregular coronas between the above mafic and Ca-Al-rich microdomains (Fig. 7a-d). Glaucophane crystals are generally elongated with no discernible optical zoning, although slight compositional variations can be detected with the microprobe (Section 6) and BSE images showing locally a brighter actinolitic rim when in contact with albite.

Finally, magnetite microcrystals are sometimes clustered and may represent pseudomorphs after a previous Fe-rich magmatic mineral (Fig. 8a and c, top left). Titanite is common and often contains relicts of rutile. Calcite is present in negligible quantities; it frequently forms late veins, 1 to 10 µm thick, which may intersect the main foliation (Fig. 7e-f bottom).

## 5. Major and trace elements chemistry of the bulk rock

Bulk rock analyses were performed on the four metabasite samples (Tab. 1). The sample RMT3A shows a low content of $SiO_2$ (42.54 wt%) and $K_2O$ (0.55 wt%), with a high content of MgO and FeO ($X_{Mg}$ = Mg/[Mg+Fe+Mn] = 0.710); $Na_2O$ is also relatively high (2.75 wt%). The normative mineral calculation, carried out via the CIPW norm, makes it possible to assess the mineralogical composition of the magmatic protolith, provided that the chemical composition of the rock has not been modified during metamorphism. The normative quantities of minerals for the RMT3A sample, converted to volume percentages (molar volumes of Holland and Powell, 2011), correspond to an undersaturated magmatic rock (setting $Fe^{3+}$ at 0.1 × $Fe_{total}$) with: 59.4 vol% plagioclase ($Or_7Ab_{30}An_{64}$); 21.9% olivine; 10.1% clinopyroxene; 6.2% nepheline; 1.3% ilmenite; 0.8% magnetite; 0.3% apatite. The average of four metabasite analyses (Bianco et al., 2015) gives similar results: 59.6 vol% plagioclase ($Or_8Ab_{36}An_{56}$); 19.1% olivine; 14.0% clinopyroxene; 4.9% nepheline; 1.3% ilmenite; 0.9% magnetite; 0.3% apatite.

The trace elements (Tab. 1) make it possible to better constrain the origin of the protolith. The chondrite-normalized REE patterns (Fig. 9a) show a slight LREE enrichment, up to 25× for La, with high ratios of LREE/HREE (e.g. $[Ce/Yb]_N$ = 1.81–2.02). The positive Eu-anomaly (average $Eu/Eu^*$ = 1.11) indicates plagioclase accumulation or segregation. These patterns are clearly intermediate between those of N-MORBs, depleted in LREE, and E-MORBs, strongly enriched in LREE. In addition, excluding the large-ion lithophile elements (LILE: e.g. K, Rb, Cs), because of their mobility during metamorphism, and the alkaline earth elements (Sr, Ba), which may be involved in diffusion processes from the neighbouring calcschists, the trace elements show contents between 10× and 4× those of the primitive mantle (Sun and McDonough, 1989; McDonough and Sun, 1995; Klein, 2004). These characteristics are similar to those of T-MORB (transition basalt between N-MORB and E-MORB: Figs. 9c, 10c, f). The Zr, Nb, Y, La, Sm, Tb, Ta, Hf and Ti contents (Tab. 1) were plotted in various discrimination diagrams to obtain information on the tectonic setting. In a first step, the Zr/Ti vs. Nb/Y diagram (Fig. 10a) was selected to define the basaltic nature of the studied rocks, which resulted in a sub-alkaline composition. The V vs. Ti/1000 diagram (Fig. 10b) indicates MORB affinity. In order to confirm the MORB typology, several discrimination diagrams (Furnes and Dilek, 2017; Xia and Li, 2019 and references therein) were considered (Fig. 10c-g). The ratios between high-field-strength elements (Fig. 10c-g) indicate that the analysed samples can be classified as T-and E-MORBs (Geshi et al., 2007; Sun and McDonough, 1989; Liu et al., 2015; Karsten et al., 1990). Noteworthy, both the

Hf/3–Th–Nb/16 triangular plot (Fig. 10g) and the Zr/Y vs. Zr diagram (Fig. 10h) assign the Rio Marina metabasites to "within plate tholeiite", related to E-MORB.

## 6. Mineral chemistry

Representative mineral analyses of the four studied samples are presented in Table 2 and Tables SM1–SM3, the latter provided as supplementary materials. The structural formulas are calculated on the basis of quantities of O and OH anions, chosen according to the mineral group: epidotes: $O_{12}(F,OH)_1$ and $Fe^{3+} = Fe_{total}$; micas: $O_{20}(OH,F)_4$, $Fe^{3+} = 0$; chlorites: $O_{20}(OH)_{16}$, $Fe^{3+} = 0$; feldspars: $O_8$, $Fe^{3+} = Fe_{total}$; pyroxenes: $O_6$, $Fe^{3+}$ value corresponding to 4 cations; amphiboles: procedure of Hawthone et al. (2012), giving a range of $Fe^{3+}$ values for which the cation distribution in the T, C, B and A sites is correct; for glaucophane, the formula with $Na_A = 0$ is preferred if $0 < Fe^{3+} < Fe_{total}$.

***Clinopyroxenes*** are mainly aegirine-augite/omphacite and their composition is highly variable with $X_{Jd}$ ranging from 0.292 to 0.122 (Fig. 11a). This variation does not correspond to a clear zoning of the crystals, but more to a chemical heterogeneity on a very small scale which could correspond to exsolution, perhaps related to the existence of a LT solvus between omphacite/aegirine and augite, but also be due to partial decomposition of aegirine/omphacite into chlorite, albite and Jd-poor clinopyroxene. The two groups around $Jd_{22}Aeg_{25}Aug_{53}$ and $Jd_9Aeg_{19}Aug_{72}$ in Figure 11a correspond to the primary Jd-rich and secondary Jd-poor pyroxenes, respectively.

***Amphiboles*** are Na-amphibole and less abundant actinolite, often located within the clinopyroxene strain shadows. Na-amphibole is almost pure glaucophane (Fig. 11b) according to the nomenclature of Hawthorne et al. (2012), with $X_{Gln}$ ranging from 0.69 to 0.99 (calculated as $Al^{VI}/[Fe^{3+}+Al^{VI}]$). A slight zoning is perceptible in the matrix crystals, with the reverse glaucophanitic substitution (i.e. $Al_{-1}[Mg, Fe^{2+}]_{+1}Ca_{+1}Na_{-1}$) operating from core to rim.

The analyses reveal two types of ***epidote***: (i) some $Fe^{3+}$-rich epidote with an $X_{Fe3+}$ ratio, calculated as $Fe^{3+}/(Fe^{3+}+Al)$, ranging from 0.217 to 0.359, which corresponds to a molar fraction of pistacite varying from 0.78 to 0.92 ($X_{ps} = Fe/[Al-2+Fe]$); (ii) clinozoisite with a lower $X_{Fe3+}$, between 0.025 and 0.176, which corresponds to an $X_{ps}$ interval of 0.31 to 0.40. $Fe^{3+}$-rich epidote is abundant in the matrix; it contains microcrystalline inclusions of the $Fe^{3+}$-poor clinozoisite, associated with muscovite, albite, calcite and quartz (Fig. 8).

The analyses reveal two different types of ***white micas***: (i) fine-grained muscovite was detected in the clinozoisite-rich pseudomorphs described above; analyses show a low Mg content, of about 0.030 atoms per formula unit (a.p.f.u.); (ii) in contrast, phengite found in the matrix has an Mg content up to 0.073 a.p.f.u.

***Plagioclase*** has an albitic composition ($Ab_{93}$ on average), both in the matrix and in the clinozoisite-rich pseudomorphs. In two samples (RMT19, RMT4A), small crystals of anorthite-rich plagioclase were also found ($An_{79–99}$).

***Chlorite*** is rich in Fe and Mg, with $X_{Mg}$, calculated as $Mg^{2+}/(Mg^{2+}+Fe^{2+}+Mn^{2+})$, around 0.93. It is classified as ripidolite according to the nomenclature of Hey (1954). ***Apatite*** is fluoroapatite with F ≈ 2.9 wt%.

## 7. $^{40}Ar/^{39}Ar$ geochronology

As previously mentioned, RMT7A was chosen among the four samples, because it contains, in the matrix, a major percentage of glaucophane minerals with minor compositional heterogeneities, in order to avoid the influence of overgrown actinolite and/or zoned glaucophane can have on the final result. The separated mineral grains were irradiated for 117 hours at the McMaster Nuclear Reactor, Canada, along with the biotite mineral standard GA1550 (99.738 ± 0.104 Ma: Renne et al., 2010). Data were corrected for mass discrimination (using a value for $^{40}Ar/^{36}Ar$ of 283, determined from a known composition calibration gas), and for system blanks measured before and after 2 analyses. Corrections for $^{37}Ar$ and $^{39}Ar$ decay since irradiation were applied and the following correction factors used for neutron-induced interference reaction: $(^{39}Ar/^{37}Ar)_{Ca}$ = 0.00065 ± 0.00000325, $(^{36}Ar/^{37}Ar)_{Ca}$ = 0.00026 ± 0.000001325, and $(^{40}Ar/^{39}Ar)_{K}$ = 0.0085 ± 0.0000425, based on analyses of Ca and K salts. Ages were calculated using the atmospheric $^{40}Ar/^{36}Ar$ ratio of 298.56 (Lee et al., 2006), and decay constants of Renne et al. (2011). This is reported at 2σ level and includes a 0.5% error on the J value.

An age of 19.8 ± 1.4 Ma is then calculated from the inverse isochron analysis of the step-heating data. This inverse isochron (Fig. 12) computes an initial $^{40}Ar/^{36}Ar$ within error of atmospheric ratio (285 ± 12), suggesting that it is not affected by argon excess. Although no plateau age can be calculated from the release spectra, the apparent ages fall between 18 and 20 Ma, similar to the isochron age, suggesting that this is the best estimate for the age of the glaucophane.

## 8. P-T modelling

P-T pseudosections are used to model the stability of mineral assemblages in the P-T space, using chemical bulk compositions that closely approximate the actual rock. The P-T pseudosection of Figure 13 is based on the bulk composition of the RMT3A metabasite (Tab. 1), converted to molar percentages. The $P_2O_5$ component was subtracted by projection onto the $P_2O_3$-free subspace from the composition of apatite, not considered in the modelling. The minor component $K_2O$ has been neglected because it mainly enters into the amphibole compositions whereas the composition-activity model used for these amphiboles does not take it into account. MnO, another minor component also incorporated into amphiboles and chlorite, has been added to FeO for the same reason. The amount of O (i.e. $Fe^{3+}$) was estimated from the structural formulas and molar amounts of peak minerals, estimated by the least-square method (see Godard, 2009); it must be borne in mind that this value could have changed during metamorphism. $H_2O$ is considered to be in excess, which seems reasonable given the abundance of hydrated minerals and the high LOI value (Tab. 1). Therefore, the modelling was carried out with the THERMOCALC software in the NCFMASHTO system, using the following bulk composition (mol%): $(SiO_2)_{47.73}$ $(Al_2O_3)_{11.17}$ $(CaO)_{10.93}$ $(MgO)_{18.17}$ $(FeO)_{7.43}$ $(Na_2O)_{2.99}$ $(TiO_2)_{0.76}$ $O_{0.82}$.

The thermodynamic dataset for the pure end-members is from Holland and Powell (2011, updated version 55). The activity-composition models used for solid solutions are: Green et al. (2007), revised by Diener and Powell (2012), for omphacitic clinopyroxenes; Holland et al. (1998) for chlorite; White et al. (2007) for garnet; Holland and Powell (1998) for epidote; Holland and Powell (2003) for plagioclase; Diener et al. (2007), revised by Diener and Powell (2012), for hornblende, actinolite and glaucophane, which can be co-stable. Lawsonite, rutile, titanite and quartz are considered pure phases.

It should be emphasized here that a P-T pseudosection must in principle apply to a homogeneous system, which is not really the case for the rocks studied, where various microdomains, presumably inherited from the magmatic protolith, have partially survived deformation and diffusion. The same mineral can be highly zoned and its composition can vary significantly from one microdomain to another (Figs. 7and 8). Normally, isopleths are used to explain changes in the mineral composition and to better constrain the P-T path of the rock studied. In our case, however, the observed heterogeneity makes this approach difficult. The $X_{Fe2+}$ and $X_{Fe3+}$ ratios of the zoned minerals are highly variable and subject to great uncertainties related to the

stoichiometric estimation of $Fe^{3+}$. The isopleths corresponding to these ratios are therefore dispersed in wide T intervals of the pseudosection and thus give little useful constraints. Two sets of isopleths have nevertheless been retained because they can provide relatively reliable information; they are based on the composition of clinopyroxene ($X_{Jd+Aeg}$ = Na/Na+Ca: blue curves in Fig. 13) and that of glaucophane ($Z_{Gln}$ = Na fraction in B site, considering $Na_A$ negligible: red curves in Fig. 13).

The pseudosection (Fig. 13) is composed of 2 to 7$^{th}$ variant P-T fields, whose corresponding mineral assemblages are indicated by abbreviations (Whitney and Evans, 2010), those in parentheses being in very low modal quantity (<1 vol%).

## 9. Discussion

The following discussion focuses on two main issues: the petrological evolution of the studied metabasites and the geodynamic implications deriving from the HP-LT reconstructed conditions.

### *9.1. Petrological evolution of the metabasites*

We focus here on the protolith, metamorphic evolution and dating of the metabasites. The microstructures observed, as well as the mineral assemblages and compositions, reveal several metamorphic stages, which are detailed here below and summarized in Table 3.

#### 9.1.1. Protolith

The protolith was a magmatic rock, with a grainy texture as evidenced by the preservation of mafic and Ca-Al-rich microdomains that would represent the former magmatic pyroxene and plagioclase, respectively. The size of the pyroxene porphyroclasts, which reach a few millimetres, gives an indication of the grain size of the protolith.

The CIPW norm suggests that the protolith was a basic rock undersaturated in silica, resulting in the presence of normative olivine and nepheline. It is likely, however, that the contents of Si and other major elements have been modified during metamorphism, when the rock was stretched and laterally segmented within calcschists. To better constrain the geochemical signature of the protolith, it is therefore preferable to consider only the immobile trace elements, like REEs and HFSEs. These imply that the protolith had a composition of T- or E-MORBs (Figs. 9 and 10c-g). The positive Eu/Eu* anomaly also indicates either plagioclase accumulation in a magmatic chamber or plagioclase segregation by flowage differentiation. Field

observations, in particular the reduced thickness of the lenses, their parallelism with the main schistosity of the host calcschists, and their interbedding with them (Fig. 5), suggest that the study metabasites could have been former dolerite sills and/or dykes, deformed together with the calcschists. This interpretation is also supported by the preserved mm-sized microdomains corresponding to the protocrystals of the magmatic rock and thus suggesting that the latter was a micro-grained rock, like a microgabbro or dolerite, rather than basalt.

9.1.2. Lawsonite blueschist metamorphic stage

As previously described, the epidote crystals present in the matrix of sample RMT3A contain poly-mineral inclusions, consisting of Czo + Ms ± Ab ± Cal ± Qz and showing regular rectangular and rhombic shapes (Fig. 8); in other samples, the same poly-mineral aggregates are included in chlorite (Fig. 7d bottom). Such a microstructure is commonly interpreted as pseudomorphs after lawsonite (e.g. Félix and Fransolet, 1972; Tsujimori et al., 2006; Groppo and Castelli, 2010; Angiboust et al., 2012; López-Carmona et al., 2014; Orozbaev et al., 2015). In our case, several points corroborate this interpretation:

(a)- These prismatic inclusions have a random orientation relative to the host single crystal of epidote (Fig. 8). They cannot therefore be interpreted as inherited cores or exsolution structures of the latter, and are thus necessarily pseudomorphs.

(b)- The outline of these pseudomorphs appears sharp in the BSE images (Fig. 8a-d), because the $Fe^{3+}$-poor clinozoisite that constitutes them (medium grey) contrasts with the host $Fe^{3+}$-rich epidote (light grey). The composition of the (Mg, Fe)-free muscovite included in the pseudomorphs also contrasts with that of Mg-rich phengite in the matrix (Section 6). These compositional differences indicate that the protomineral did not contain Fe and Mg, corroborating the hypothesis that it was lawsonite.

(c)- The apparent shapes of these pseudomorphs grade between rectangles (2 in Fig. 8b, d) and rhombs (1 in Fig. 8b, d), which respectively correspond to longitudinal and basal sections of rhombic prisms. The inclusions of muscovite and albite are parallel to the long side of the rectangular longitudinal sections, thus to the prism elongation, whereas they are preferentially oriented parallel to one of the diagonals of the basal rhombic sections (see red lines in Fig. 8b, d), which means that the two diagonals were not crystallographically equivalent. This strongly suggests that the protocrystals were orthorhombic prisms with {110} faces, which is a common habit of lawsonite.

In addition to the pseudomorphs after lawsonite, the single crystals of epidote contain micro-inclusions of euhedral glaucophane, apatite and titanite with scarce relicts of rutile (Fig. 8). Moreover, the same epidote crystals show elongated sheet-like zones that appear brighter in BSE, being richer in $Fe^{3+}$ (barely visible in Fig. 8c). Since these zones are positioned in the prolongation of chlorite sheets of the matrix, they resulted from the replacement of chlorite that occupied, probably with other minerals, the interstices between the prisms of lawsonite and glaucophane. Thus, the first recognizable metamorphic paragenesis consisted of lawsonite, glaucophane, chlorite, apatite, titanite and/or rutile and possibly a little phengite in the Ca- and Al-rich microdomains after plagioclase, whereas the mafic microdomains after pyroxene were likely already transformed into omphacite/aegirine, as suggested by the pseudosection (see below). Clusters of iron oxides could be derived from another mineral, such as spinel or iddingsite, a Fe-rich and Si-poor form of olivine alteration.

This paragenesis, which predates epidote, must have been formed under the HP conditions of the lawsonite-blueschist subfacies (e.g. Evans, 1990). In the P-T pseudosection, the mineral assemblages with Chl + Lws + Gln + Omp+ Rt/Ttn ± Act appear stable at high pressure, beyond a limit ranging from 1.2 GPa–400°C to 2.0 GPa–550°C (Table 3 and Fig. 13). Some considerations, with the due approximation, make it possible to restrict these conditions: (i) the P-T conditions cannot have exceeded 2.0 GPa–550°C, since garnet, which was not observed in these rocks, should have appeared in such conditions; (ii) the presence of relict rutile within a few titanite crystals (Fig. 6f) suggests that rutile-bearing fields have been reached (i.e. “Chl (Act) Gln Omp Lws Rt" or “Chl Gln Omp Lws Rt" in Fig. 13); (iii) the isopleths $Z_{Gln}$ applied to the early glaucophane enclosed within epidote ($Z_{Gln}$ = 0.919 ± 0.027 [1σ]), despite the reservations about their reliability, suggest temperatures around 460°C (Fig. 13). We can therefore support for the following conditions at this stage of metamorphism: 450°C < T < 500°C; P > 1.6 GPa, significantly higher than those obtained previously by the conventional geothermobarometric approach and which are listed in Figure 1a.

Both the glaucophane crystals and pseudomorphs after lawsonite included in one and the same epidote monocrystal have no clear preferential orientation, being almost randomly oriented (Fig. 8). This suggests that deformation was not intense at this stage.

9.1.3. Epidote blueschist stage

The breakdown of lawsonite into Czo + Ms ± Ab ± Cal ± Qz cannot occur in a closed system. Indeed, it requires some interaction with other minerals present in the matrix (e.g. Orozbaev et al., 2015) and the mobility of alkalis. We have balanced a possible metamorphic reaction, assuming the mobility of alkalis and water:

1 Lws $[Si_2Al_2CaO_7(OH)_2.H_2O]$ + 0.083*x* $K_2O$ + 0.050(1-*x*) $Na_2O$ =

0.500 Czo $[Si_3Al_3Ca_2O_{12}(OH)_1]$ + 0.167*x* Ms $[Si_3Al_3K_1O_{11}(OH)_2]$ + 0.100(1-*x*) Ab $[NaAlSi_3O_8]$ + 0.200(1-*x*) Ky $[SiAl_2O_5]$ + (1.750 - 0.167*x*) $H_2O$, with $0 < x < 1$.

Such a theoretical reaction produces clinozoisite, muscovite and albite, as observed in the pseudomorphs, and could thus approach reality.

In addition to the replacement of lawsonite by clinozoisite, growth of epidote (pistacite) encompassing both lawsonite pseudomorphs and glaucophane crystals is observed in the Ca- and Al-rich microdomains (Fig. 8). This epidote is in equilibrium with ubiquitous glaucophane, which tends to concentrate in coronas between the Al-rich and mafic microdomains, as its growth required the inputs of Al and Na from the Al-rich microdomains (i.e. the matrix) and of Fe and Mg from the mafic microdomains (i.e. the pyroxene porphyroclasts).

The mineralogical assemblages observed at this metamorphic stage are typical of the epidote-blueschist subfacies (e.g. Evans, 1990). The P-T pseudosection of Figure 13 shows that the transition between the above lawsonite-bearing stage and this new epidote stage occurs in a narrow P-T strip, about 0.05-GPa wide between 1.1 GPa–400°C and 1.9 GPa–540°C, consisting of various multivariant P-T fields where lawsonite and epidote coexist. We calculated the modal quantities of the minerals, expressed in volume percentages, at two P-T points of the pseudosection (dots in Fig. 13), before and after the transition:
1.6 GPa, 475°C (vol%): 15.0 Gln + 0.6 Act + 24.9 Omp + 30.2 Chl + 28.6 Lws + 0.0 Ep + 0.7 Rt + 0.0 Ttn;
1.5 GPa, 480°C (vol%): 34.3 Gln + 2.0 Act + 4.9 Omp + 28.1 Chl + 0.0 Lws + 28.7 Ep + 0.0 Rt + 2.0 Ttn.

These results properly account for several petrological observations: (i) the transformation of lawsonite into epidote; (ii) the replacement of rutile by titanite, the P-T fields where titanite is stable being wider after the transition than before (Fig. 13); and most importantly (iii) the growth of glaucophane (Gln), and incidentally of actinolite (Act), at the expense of omphacitic pyroxene (Omp), thus explaining the presence

of glaucophane around, as well as in the strain shadows and fractures of the pyroxene porphyroclasts (Fig. 7). However, the growth of glaucophane at the expense of pyroxene was not as complete as predicted by the model, since ideally the amount of pyroxene should have reduced down to ~4.9 vol% at this stage. This reflects a lack of equilibrium at the global level of the rock, as already emphasized.

The assemblage Chl + Gln + Act + Omp + Ep + Ttn corresponds to temperatures of about 450–520°C for a pressure that can range from 1.5 to 0.9 GPa without notable modification of the mineral paragenesis. The zoning of amphibole crystals, with a slight decrease in the glaucophane end-member from core to rim, suggests an evolution at decreasing P and/or increasing T. Applying the $Z_{Gln}$ isopleths to the average compositions of the cores ($Z_{Gln}$ = 0.900 ± 0.025 [1σ]) and rims (0.871 ± 0.049) of glaucophane crystals in the matrix confirms such an evolution up to around 520°C. Under these conditions, the model predicts an $X_{Jd+Aeg}$ ratio of 0.46 for the clinopyroxene, which is consistent with the composition observed (Fig. 11a), if care is taken to exclude the values close to 0.30 that result from late albite exsolution.

The albitic plagioclase ($Ab_{93}$) occurring, locally, in the pseudomorphs after lawsonite (Fig. 8) is stable only at pressures lower than the dashed curve of Figure 13, corresponding to the equilibrium $Ab_{93}$ = $Jd_{100}$ + Qz, and hence at pressures below the lawsonite-epidote transition. It is possible that lawsonite remained metastable for a certain time during decompression or, alternatively, that albite developed secondarily from an Na-rich HP mineral like paragonite, common in such pseudomorphs (e.g. Félix and Fransolet, 1972; Groppo and Castelli, 2010; López-Carmona et al., 2014; Orozbaev et al., 2015).

Since much of the glaucophane developed and deformed during this stage, the date of 19.8 ± 1.4 Ma is likely to be related to the lawsonite-epidote transition, after the pressure peak. Since this glaucophane developed in fractures and strain shadows of pyroxene porphyroclasts (Fig. 7), most of the deformation probably occurred at this stage.

9.1.4. Greenschist-facies retrogression

The retrograde evolution is documented by the following features: (i) thin symplectites replacing omphacite (Fig. 7), as a consequence of the reaction Omp → Di + Chl + Qz + Ab; (ii) the general development of albite ($Ab_{93}$) in the matrix (Fig. 7); (iii) the transformation of glaucophane into chlorite and calcic amphibole, particularly actinolite, on its borders and along fractures (Fig. 7).

This stage is characterized by Ep + Act + Ab + Chl + Di + Ttn as the main paragenesis, and thus indicates retrogression in greenschist-facies conditions. The pseudosection (Figure 13) indicates that, while glaucophane disappears, plagioclase and calcic amphiboles appear around 470–510°C, at P < 0.9 GPa. Under these conditions, the plagioclase predicted by the model ($Ab_{92}$) has a composition close to that observed ($Ab_{93}$).

9.1.5. Late high-temperature imprint

The mm-sized crystals of anorthite observed in the matrix of some of the metabasite samples (Fig. 6e) may have replaced some former epidote, which is quite common (e.g. Holdaway, 1972). Whatever its origin, this anorthite suggests a late increase in temperature, probably due to the emplacement at 6.53 Ma of the Porto Azzurro granite pluton (Gagnevin et al., 2011) at shallow crustal levels, as documented by thermobarometric studies on the metamorphic aureole (0.2 GPa at 300–600°C: Pertusati et al., 1993; <0.2 GPa at 550–600°C: Musumeci and Vaselli, 2012; 6.5 ± 0.9 km at 630°C: Caggianelli et al., 2018).

### *9.2. Geodynamic implications*

The study of the metabasites embedded in the calcschists leads to the following considerations:

(a) Despite probable chemical exchanges with the host calcschists, the immobile elements of the metabasites reveal an affinity with T- and E-MORBs (Figs. 9c, 10c-g). Moreover, calcschists with interbedded metabasites, together with serpentinites at their top and radiolarites at their base (Fig. 3), appear to be a kind of "Steinmann trinity" exhibiting many features of ophiolites. As already suggested by Duranti et al. (1992), Pertusati et al. (1993), Bortolotti et al. (2001) and Pandeli et al. (2001), these rocks could have belonged to the lithosphere of the Piedmont-Ligurian palaeo-ocean, which disappeared by subduction during Cretaceous-Eocene time (Boccaletti et al., 1971; Carosi and Montomoli, 2002; Molli, 2008). However, this hypothesis is hampered by the fact that the radiolarites are in succession with carbonatic platform rocks (Fig. 3a), and by the age of the neighbouring metasediments, which contain early Oligocene detrital zircons (31.6 ± 0.5 Ma: Jacobs et al., 2018; see above). The metabasite protolith, likely a micrograbbro or dolerite with T/E-MORB affinity (Figs. 9c, 10c-g), may also have belonged to an atypical oceanic crust, such as a back-arc basin. This hypothesis is however poorly compatible with the Oligocene age of the detrital zircons in the metasediments, since subduction was already affecting the Adria plate during Oligocene, making it difficult

to reconcile with a back-arc basin on the Adria margin (see Molli, 2008 for a review). Alternatively, the study rocks could be mafic bodies deriving from a mantle magma injected into the thinned Adria continental crust, in agreement with the discrimination diagrams (Fig. 10g-h). Accepting this latter view, the calcschists and metabasites could be related to the lower part of the Scaglia Toscana Fm., deposited from late Cretaceous to Oligocene in the continental Tuscan Domain (Canuti et al., 1965; Kälin et al., 1979; Fazzuoli et al., 1996; Brogi et al., 2000; Bambini et al., 2009). Alternatively, this succession could be referred to the Canetolo Unit (Sub-Ligurian Units), even if its Cretaceous age has never been documented although not excluded (Perilli et al., 2009 and references therein).

(b) Metabasites have undergone HP-LT blueschist-facies metamorphism, as evidenced by the presence of omphacite, glaucophane and especially pseudomorphs after lawsonite (Fig. 8). Thermodynamic modelling indicates conditions of more than 1.6 GPa and 450–500°C at maximum depth, corresponding to a gradient of ~280°C/GPa (i.e. ~8°C/km) typical of subduction zones (Ernst et al., 2007; Yamato et al., 2007 and references therein). Pandeli et al. (2001) obtained lower P-T estimates for the host phengite-bearing calcschists (>0.8 GPa, ~300°C), although still consistent with an HP-LT gradient. The abundance of calcite and the absence of aragonite in these rocks indicate a readjustment below the univariant curve Arg=Cal (Fig. 14). It seems that the calcschists have more easily re-equilibrated than the metabasites during retrogression, because of the extreme ease with which carbonates deform and recrystallize.

(c) The glaucophane dating yields an age of 19.8 ± 1.4 Ma ($^{40}Ar/^{39}Ar$ method). Most of this glaucophane is syn-kinematic and the pseudosection modelling indicates that it formed after the pressure peak during the lawsonite-epidote transition (Fig. 13). The portion of glaucophane preserved as relicts in the epidote and coeval with lawsonite is negligible in volume in comparison with the glaucophane present in the matrix and formed at the same time as the epidote, so that only this latter glaucophane actually contributes to the age obtained. Although the dated sample shows glaucophane without clear actinolitic zoning, partial readjustment of glaucophane and late actinolite formation cannot be totally ruled out. Therefore, the age obtained can be interpreted as the minimum age to be connected to the epidote blueschist stage. The glaucophane age is in good agreement with the $^{40}Ar/^{39}Ar$ dating carried out on syn-kinematic phengite defining the main schistosity of the host calcschists (19.68 ± 0.15 Ma: Deino et al., 1992). This early Miocene episode occurred after the peak pressure, coeval with the main phase of deformation, and preceding

the exhumation. Similar early Miocene ages of HP-LT metamorphism are also reported in Brunet et al. (2000) on the mainland (Fig. 1). On the contrary, an older HP-age (25 ± 0.3 Ma: Rossetti et al., 2001) was documented for the Gorgona Island (Fig. 1), thus suggesting a continuous but diachronous deformational phase.

(d) The metabasites record a retrograde evolution, without significant deformation, under greenschist-facies conditions, and then underwent a LP heating episode attributable to the intrusion of the Porto Azzurro monzogranite (Caggianelli et al., 2018). The exhumation to the retrograde evolution occurred during the middle Miocene, being consecutive to the collision and preceding the monzogranite intrusion (~ 6.5 Ma).

Whether the studied rocks belonged to an atypical oceanic lithosphere, whether they were injected into the thinned continental crust of Adria, or whether they belonged to the Cretaceous-Oligocene sub-Ligurian domain defined as being intermediate between the oceanic and continental domains (Cerrina-Feroni et al., 1991, Plesi et al., 1993), these seemingly divergent hypotheses basically reflect the same reality, namely the belonging of the study area to the margin of the Adria microplate, dragged into subduction during Oligocene, before reaching, at the beginning of the Miocene, HP conditions similar to those documented for Gorgona Island, Argentario Promontory and Giglio Island, where comparable lawsonite-bearing glaucophanites are also described (Fig. 1, e.g. Theye et al., 1997; Brunet et al., 2000; Rossetti et al., 2001). Further studies are however needed to investigate whether HP metamorphism affected the entire tectonic pile underneath the studied calcschists of the Elba Island.

## 10. Conclusions

The metabasites interbedded and stretched in calcschists at Rio Marina (Eastern Elba Island) are possibly derived from dykes and/or sills with T/E-MORB geochemical affinity. The oldest preserved metamorphic paragenesis (Chl + Lws + Gln + Omp + Rt) reflects HP-LT metamorphic conditions with P ≥ 1.6 GPa and 450–500°C, which correspond to subduction down to ca. 60 km depth (Fig. 14). Much of the glaucophane blastesis took place during a deformation episode at the lawsonite-epidote transition, within the blueschist facies, this episode, attributed to the early Miocene by the dating of glaucophane (19.8 ± 1.4 Ma), postdates the peak pressure. Gorgona Island, the eastern coast of Elba, the Argentario Promontory and Giglio Island contain serpentinites, metasediments and lawsonite-bearing glaucophanites (Fig. 1a). This NW-SE trending

area, about 150 km long, thus seems to constitute a HP-LT metamorphic belt, largely masked by the Tyrrhenian Sea, and many of the conclusions of this study are likely applicable to the whole of this belt. With the subsequent exhumation, which was favoured by the extensional tectonics, the metabasites of Rio Marina were affected by retrograde metamorphism under greenschist-facies conditions. Finally, the intrusion of the Porto Azzurro pluton, during late Miocene, resulted in a weak imprint of LP thermal metamorphism, revealed by the local appearance of anorthite. In this framework, the eastern Elba Island continental units are attributed to the thinned margin of the Adria plate.

## Acknowledgments

This research has received funding from the European Union's Seventh Framework Program under grant agreement n° 608553 (project IMAGE). We want remember Marco Meccheri that passed away a few years ago, who participated to the discovery and study of such metabasites. Our thoughts go to him and his enthusiasm. Suggestions and criticisms from two anonymous referees helped us to improve the original manuscript. Stereograms were drawn using the free software STEREONET 10.0.0 by R.W. Allmendinger (http://www.geo.cornell.edu/geology/faculty/RWA/).

## Figure and Table Captions

Fig. 1 – Structural sketch map of inner Northern Apennines and Corsica with HP-LT metabasites (black circles) and metasediments (blue circles). P-T values and ages for the Northern Apennines are from Kligfield et al. (1986), Theye et al. (1997), Giorgetti et al. (1998), Brunet et al. (2000), Rossetti et al. (1999), Rossetti et al. (2001), Elter and Pandeli (2002), Brogi and Giorgetti (2012); Bianco et al. (2015) and from this study (n° 13). P-T values and ages for the Corsica area are from Brunet et al. (2000); Rossetti et al. (2002), Vitale et al. (2011); Vitale and Herwartz (2013), Rossetti et al. (2015) with references therein. The Gorgona, Giglio and Elba Islands with other minor islands are referred to as the Tuscan Archipelago in the main text.

Fig. 2 – Geological sketch map of Elba Island. The tectonic units and their relationships are modified after Bianco et al. (2015). The Rio Marina area, where the metabasites occur, is indicated by the black frame.

Fig. 3 – Tectono-stratigraphic pile of Elba Island. (a) Tectono-stratigraphic logs of the different tectonic units belonging to continental and oceanic settings; (b) detail of the upper part of the Continental Unit 2 (a-d: see text).

Fig. 4 – Geological map and cross-sections of the Rio Marina area

Fig. 5 – Sampling area in the Rio Marina harbour; (a) metabasite lenses embedded in calcschists. The lenses follow the main schistosity, gently NW/SW-dipping; inset: equal-angle stereographic projection in the lower hemisphere of the poles of the measured main schistosity; (b, c) metabasites laterally segmented at different scales within calcschists; (d) sampled metabasites; (e) tight and highly non-cylindrical isoclinal folds in calcschists.

Fig. 6 – Microphotographs and BSE image of the studied metabasites and calcschists. Plane-polarized light (c, d, e), cross-polarized light (a, b, g) and BSE image (f); (a)- calcschists with elongated crystals of phengite, quartz and calcite; (b)- core and mantle microstructures in calcschists, indicating progressive recrystallization of calcite and quartz; (c)- fractured porphyroclast of clinopyroxene with glaucophane and actinolite in the strain shadows in metabasites; (d)- large glaucophane crystals in the matrix of metabasite; (e)- altered rock portion of metabasites with abundant titanite and anorthite testifying overprint of low-P thermal metamorphism; (f)- large titanite including rutile crystals in metabasite; (g)- epidote crystals in metabasite, enclosing glaucophane, albite and clinozoisite after lawsonite (see Fig. 8).

Fig. 7 – Pyroxene porphyroclasts within metabasites. Metabasite samples RMT19 (a, b, e, f) and RMT4A (c, d); red-green-blue (RGB) images (b, d, f) constructed from the first 3 main components obtained by PCA of chemical element maps and BSE images (a, c, e). (a, b)- Clinopyroxene porphyroclast, almost completely replaced by symplectites composed of Di + Chl + Qz + Ab + Gln, is fractured and stretched in a matrix mainly composed of epidote and chlorite; glaucophane is concentrated in the strain shadow of the porphyroclast. (c, d)- Clinopyroxene partially transformed into symplectite (top) in a matrix with epidote, titanite and chlorite (bottom); glaucophane is concentrated in a corona between clinopyroxene and its matrix; clinozoisite crystals with prismatic forms (bottom) are pseudomorphs after lawsonite (see text). (e, f)- Stretched and fractured clinopyroxene porphyroclast showing fractures filled with glaucophane and chlorite; the late fracture at bottom is filled with calcite.

Fig. 8 – Pseudomorphs after lawsonite in single crystals of epidote. Metabasite sample RMT3A; RGB images (c, f; see Fig. 7 for the technique) and BSE images (a, b, d, e). Rhombic basal sections (1) and rectangular longitudinal sections (2) of former lawsonite prisms replaced by $Fe^{3+}$-poor clinozoisite, basal

sections of glaucophane (3), apatite (4) and titanite (not visible) are all enclosed in single crystals of $Fe^{3+}$-rich pistacite (5). The inclusions of muscovite, albite and calcite (dark gray) in pseudomorphs after lawsonite are preferentially oriented (red lines), suggesting an orthorhombic symmetry for the protomineral (see text). White mica is phengite in the matrix and muscovite in the pseudomorphs; glaucophane becomes actinolite along the fractures.

Fig. 9 – Spider diagrams for the Rio Marina metabasites. (a) REE spider diagram normalized to chondrite (McDonough and Sun, 1995); (b) Multi-elements spider diagram normalized to E-MORB (Sun and McDonough, 1989); (c) REE spider diagram normalized to T-MORB (Klein, 2004).

Fig. 10 – Discriminant geochemical diagrams for the Rio Marina metabasites. Circles represent the studied metabasites. (a, b)- Zr/Ti vs. Nb/Y and V vs. Ti/1000 diagrams, from Furnes and Dilek (2017); (c)- Zr/Y vs. Nb/Y diagram, from Ueda et al. (2000); (d)- Y/Nb vs. Zr/Nb diagram; (e)- ternary diagram 3×Tb–Th–2×Ta; (f)- $(La/Sm)_N$ vs. Zr/Nb diagram, La/Sm being normalized to primitive mantle (Sun and McDonough, 1989); (g)- ternary diagram Hf/3–Th–Nb/16; (h): Zr/Y vs. Zr diagram. Diagrams (d) to (h) are from Xia and Li (2019). All values are in µg/g (i.e. ppm). Symbols: N-, T-, E-, P-MORBs are normal, transitional, enriched and plume-type MORBs, respectively; PIAT: Primitive Island Arc Tholeiite; ICA: Island Arc Calc-alkaline Basalt; IAT: Island Arc Tholeiites; BA: Back Arc; CT: Continental Tholeiites; CA: Continental Alkali-Basalt; TR: Transitional series; TH: Tholeiitic series; ALK: Alkaline series; WPA: Within-plate alkaline basalt; WPT: Within-plate Tholeiites; WPB: Within-plate Basalts; IAB: Island Arc basalts; OIB: Oceanic Island Basalt; OPB: Oceanic Plateau Basalt;

Fig. 11 – Clinopyroxene and amphibole compositions in RMT3A metabasite sample. (a) Clinopyroxene compositions in the augite (Di, En, Fs, Hd)–jadeite–aegirine ternary diagram; (b) glaucophane analyses plotted in the diagram for Na-amphiboles (Hawthorne et al., 2012).

Fig. 12 – Glaucophane geochronology. (a) Inverse isochron correlation plot (MWSD: Mean Weight Square Deviates); (b) step-heating release spectra. Data are listed in Table SM4 of the supplementary materials.

Fig. 13– P-T pseudosection of the Rio Marina metabasites. Modelling is based on the composition of sample RMT3A (see text). Fluid (pure $H_2O$) is assumed in excess. Stable assemblage fields are coloured by variance. Red and yellow lines are, respectively, the isopleths for the molar fraction of the glaucophane end-member in amphibole ($Z_{Gln}$ = Na in $M_4$) and the jadeite-aegirine fraction in clinopyroxene ($X_{Jd+Aeg}$ = Na/Na+Ca). Dashed line is the stability limit for plagioclase $Ab_{92}$ (see text). Green and yellow dots represent the P-T points, before and after the lawsonite-epidote transition respectively, at which the modal quantities of the minerals are calculated (see text).

Fig. 14 – Geological evolution of Elba Island. The evolution is illustrated through sketched cross-sections related to specific steps of the P-T-t path deduced from this study. The Arg=Cal curve is calculated using the thermodynamic dataset of Holland and Powell (2011; version 55); the other P-T boundaries are reported from Figure 13; red dots: ages of glaucophane and the Porto Azzurro pluton intrusion; light green star: studied rocks from Rio Marina.

Table 1 – Bulk-rock (wt%) and trace element (μg/g) compositions of Rio Marina metabasite samples RMT3A, RMT4A, RMT7A, RMT19A

L.O.I.: loss on ignition.

Table 2 – Representative microprobe analyses for metabasite sample RMT3A

av(*n*): average of *n* analyses; *: total without $H_2O$, with $FeO_{total}$ and subtraction of O≡F; **: glaucophane within epidote; ***: in the matrix; ****: in pseudomorphs after lawsonite.

Table 3 – Main mineral assemblages and microstructures in the Rio Marina metabasites.

## Supplementary materials

Table SM1 – Representative microprobe analyses for metabasite sample RMT19

Av(n): average of n analyses.

Table SM2 – Representative microprobe analyses for metabasite sample RMT4A

Av(n): average of n analyses.

Table SM3 – Representative microprobe analyses for metabasite sample RMT7A

Av(n): average of n analyses.

Table SM4 – $^{40}Ar/^{39}Ar$ step-heating experiments on glaucophane contained in the sample RMT7A. *J = 0.00858296 +/- 0.0000429148.

## References


Achiardi, G. D', 1896. Il granato dell'Affaccata, nell'isola d'Elba. Annali delle Università toscane XX, 3–26.

Angiboust, S., Langdon, R., Agard, P., Waters, D., Chopin, C., 2012. Eclogitization of the Monviso ophiolite (W. Alps) and implications on subduction dynamics. Journal of Metamorphic Geology 30, 37–61.

Bambini, A.M., Brogi, A., Cornamusini, G., Costantini, A., Lazzarotto, A., 2009. Nuovi dati litostratigrafici e biostratigrafici sulla Scaglia toscana nella Toscana meridionale (Area di Rapolano Terme). Bollettino della Società Geologica Italiana 128, 669–693.

Barchi, M.R., 2010. The Neogene-Quaternary evolution of the Northern Apennines: crustal structure, style of deformation and seismicity. In: Beltrando, M., Peccerillo, A., Mattei, M., Conticelli, S., Doglioni, C. (Eds.), The Neogene-Quaternary Evolution of the Northern Apennines: Crustal Structure, Style of Deformation, Seismicity. Journal of the Virtual Explorer 36(10) [//virtualexplorer.com.au/journal].

Bianco, C., Brogi, A., Caggianelli, A., Giorgetti, G., Liotta, D., Meccheri, M., 2015. HP-LT metamorphism in Elba Island: Implications for the geodynamic evolution of the inner Northern Apennines (Italy). Journal of Geodynamics 91, 13–25.

Boccaletti, M., Elter, P., Guazzone, G.J.P., 1971. Plate tectonic models for the development of the western Alps and Northern Apennines. Nature 234, 108–111.

Bortolotti, V., Fazzuoli, M., Pandeli, F., Principi, G., Babbini, A., Corti, S., 2001. Geology of Central and Eastern Elba Island Italy. Ofioliti 26, 97–150 [+ 79–96].

Bortolotti, V., Pandeli, E., Principi, G., 2015. Carta geologica dell'Isola d'Elba, scala 1:25.000. Note illustrative/Geological Map of Elba Island, 1:25.000 Scale. Explanatory notes, D.R.E.A.M., 74 pp.

Brogi, A., 2008. Kinematics and geometry of Miocene low-angle detachments and exhumation of the metamorphic units in the hinterland of the Northern Apennines (Italy). Journal of Structural Geology 30, 2–20.

Brogi, A., Cornamusini, G., Costantini, A., Di Vincenzo, G., Lazzarotto, A., 2000. Cretaceous volcanism of the southern Tuscany: record of volcanic bodies from Tuscan succession of Rapolano Terme. Memorie della Società Geologica Italiana 55, 329–337.

Brogi, A., Giorgetti, G., 2012. Tectono-metamorphic evolution of the siliciclastic units in the Middle Tuscan Range (inner Northern Apennines): Mg-carpholite bearing quartz veins related to syn-metamorphic syn-orogenic foliation. Tectonophysics 526–529, 167–184.

Brogi, A., Liotta, D., 2008. Highly extended terrains, lateral segmentation of the substratum, and basin development: The middle-late Miocene Radicondoli Basin (inner northern Apennines, Italy). Tectonics 27, 1–20.

Brunet, C., Monié, P., Jolivet, L., Cadet, J.P., 2000. Migration of compression and extension in the Tyrrhenian Sea, insights from $^{40}Ar/^{39}Ar$ ages on micas along a transect from Corsica to Tuscany. Tectonophysics 321, 127–155.

Caggianelli, A., Zucchi, M., Bianco, C., Brogi, A., Liotta, D., 2018. Estimating PT metamorphic conditions on the roof of a hidden granitic pluton: an example from the Mt. Calamita promontory (Elba Island, Italy). Italian Journal of Geosciences 137, 238–253.

Canuti, P., Focardi, P., Sestini, G., 1965. Stratigrafia, correlazione e genesi degli Scisti Policromi dei Monti del Chianti (Toscana). Bollettino della Società Geologica Italiana 84(6), 93–166.

Carmignani, L., Decandia, F.A., Disperati, L., Fantozzi, P.L., Lazzarotto, A., Liotta, D., Meccheri, M., 1994. Tertiary extensional tectonics in Tuscany (Northern Apennines, Italy). Tectonophysics 238, 295–315.

Carmignani, L., Conti, P., Cornamusini, G., Meccheri, L., 2004. The internal Northern Apennines, the northern Tyrrhenian Sea and the Sardinia-Corsica block. International Geological Congress 32, 59–77.

Carosi, R., Montomoli, C., 2002. Strutture tardo orogeniche e compressione parallela all'orogene in Appennino Settentrionale: la struttura di interferenza polifasica di S. Giuliano (Unità di Santa Maria del Giudice, Monti Pisani). Atti della Società Toscana di Scienze Naturali, Memorie Serie A, 2000-2001, 61–68.

Cerrina-Feroni, A., Martinelli, P., Perilli, N.M.L., 1991. Stratigrafia e struttura dell'Unità di Canetolo in Val Cedra (Appennino parmense). Memorie Descrittive della Carta Geologica d'Italia 46, 301–312.

Deino, A., Keller, J.V.A., Minelli, G., Pialli, G., 1992. Datazioni $^{39}Ar/^{40}Ar$ del metamorfismo dell'Unità di Ortano-Rio Marina (Isola d'Elba): risultati preliminari. Studi Geologici Camerti 1, 187–192.

Diener, J.F.A., Powell, R., 2012. Revised activity-composition models for clinopyroxene and amphibole. Journal of Metamorphic Geology 30, 131–142.

Diener, J.F.A., Powell, R., White, R.W., Holland, T.J.B., 2007. A new thermodynamic model for clino- and ortho-amphiboles in the system $Na_2O–CaO–FeO–MgO–Al_2O_3–SiO_2–H_2O–O$. Journal of Metamorphic Geology 25(6), 631–656.

Dini, A., Innocenti, F., Rocchi, S., Tonarini, S., Westerman, D.S., 2002. The magmatic evolution of the late Miocene laccolith-pluton-dyke granitic complex of Elba Island, Italy. Geological Magazine 139, 257–279.

Duranti, S., Palmeri, R., Pertusati, P.C., Ricci, C.A., 1992. Geological evolution and metamorphic petrology of the sequences of eastern Elba (Complex II). Acta Vulcanologica 2, 213–229.

Elter, F. M., Pandeli, E. 2002. The HP-LP meta-ophiolitic unit and Verrucano of the Cala Grande area in the Argentario Promontory (Southern Tuscany, Italy): structural-metamorphic evolution and regional considerations. Ofioliti, 27(2), 91–102.

Ernst, W.G., Tsujimori, T., Zhang, R., Liou, J.G., 2007. Permo-Triassic collision, subduction-zone metamorphism, and tectonic exhumation along the East Asian continental margin. Annual Review of Earth and Planetary Sciences 35, 73–110.

Evans, B.W., 1990. Phase relations of epidote-blueschists. Lithos 25, 3–23.

Fazzuoli, M., Pandeli, E., Sandrelli, F., 1996. Nuovi dati litostratigrafici sulla Scaglia Toscana (scisti policromi) dei Monti del Chianti (Appennino settentrionale). Atti della Società Toscana di Scienze Naturali, Memorie Serie A 103, 95–104.

Félix, C., Fransolet, A.M., 1972. Pseudomorphes à epidote s.l., paragonite, muscovite s.l., chlorite, albite,...de porphyroblastes de lawsonitedans les glaucophanites de l'île de Groix (Bretagne - France). Annales de la SociétéGéologique de Belgique 95, 323–334 [+ 345–391].

Furnes, H., Dilek, Y., 2017. Geochemical characterization and petrogenesis of intermediate to silicic rocks in ophiolites: A global synthesis. Earth-Science Reviews 166, 1–37.

Gagnevin, D., Daly, J.S., Horstwood, M.S.A., Whitehouse, M.J., 2011. In-situ zircon U-Pb, oxygen and hafnium isotopic evidence for magma mixing and mantle metasomatism in the Tuscan Magmatic Province, Italy. Earth and Planetary Science Letters 305, 45–56.

Geshi, N., Umino, S., Kumagai, H., Sinton, J.M., White, S.M., Kisimoto, K., Hilde, T.W., 2007. Discrete plumbing systems and heterogeneous magma sources of a 24 $km^3$ off-axis lava field on the western flank of East Pacific Rise, 14 S. Earth and Planetary Science Letters 258, 61–72.

Gillet, P., Goffé, B., 1988. On the significance of aragonite occurrences in the Western Alps. Contributions to Mineralogy and Petrology 99, 70–81.

Giorgetti, G., Goffé, B., Memmi, I., Nieto, F., 1998. Metamorphic evolution of Verrucano metasediments in Northern Apennines; new petrological constraints. European Journal of Mineralogy 10, 1295–1308.

Godard, G., 2009. Two orogenic cycles in eclogite-facies gneisses of the Southern Armorican Massif (France). European Journal of Mineralogy 21, 1173–1190.

Green, E., Holland, T., Powell, R., 2007. An order-disorder model for omphacitic pyroxenes in the system jadeite-diopside-hedenbergite-acmite, with applications to eclogitic rocks. American Mineralogist 92(7), 1181–1189.

Groppo, C., Castelli, D., 2010. Prograde P-T evolution of a lawsonite eclogite from the Monviso meta-ophiolite (Western Alps): dehydration and redox reactions during subduction of oceanic FeTi-oxide gabbro. Journal of Petrology 51, 2489–2514.

Hawthorne, F.C., Oberti, R., Harlow, G.E., Maresch, W.V., Martin, R.F., Schumacher, J.C., Welch, M.D., 2012. Nomenclature of the amphibole supergroup. American Mineralogist 97, 2031–2048.

Hey, M.H., 1954. A new review of the chlorites. The Mineralogical Magazine and Journal of the Mineralogical Society 30, 278–292.

Holdaway, M.J., 1972. Thermal stability of Al-Fe epidote as a function of $fO_2$ and Fe content. Contributions to Mineralogy and Petrology 37, 307–340.

Holland, T.J.B., Powell, R., 1998. An internally consistent thermodynamic data set for phases of petrological interest. Journal of metamorphic Geology 16, 309–343.

Holland, T.J.B., Powell, R., 2003. Activity–composition relations for phases in petrological calculations: an asymmetric multicomponent formulation. Contributions to Mineralogy and Petrology 145(4), 492–501.

Holland, T.J.B., Powell, R., 2011. An improved and extended internally consistent thermodynamic dataset for phases of petrological interest, involving a new equation of state for solids. Journal of Metamorphic Geology 29, 333–383.

Holland, T.J.B., Baker, J.M., Powell, R., 1998. Mixing properties and activity-composition relationships of chlorites in the system MgO-FeO-$Al_2O_3$-$SiO_2$-$H_2O$. European Journal of Mineralogy 10, 395–406.

Jacobs, J., Paoli, G., Rocchi, S., Ksienzyk, A.K., Sirevaag, H., Elburg, M.A., 2018. Alps to Apennines zircon roller coaster along the Adria microplate margin. Scientific reports 8, 2704, doi: 10.1038/s41598-018-20979-w.

Jolivet, L., Faccenna, C., Goffé, B., Mattei, M., Rossetti, F., Brunet, C., Storti, F., Funiciello, R., Cadet, J.P., D'Agostino, N., Parra, T., 1998. Midcrustal shear zones in postorogenic extension: example from the northern Tyrrhenian Sea. Journal of Geophysical Research: Solid Earth 103, 12123–12160.

Kälin, O., Patacca, E., Renz, O., 1979. Jurassic pelagic deposits from Southeastern Tuscany; aspects of sedimentation and biostratigraphic data. Eclogae Geologicae Helvetiae 72, 715–762.

Karsten, J.L., Delaney, J.R., Rhodes, J.M., Liias, R.A., 1990. Spatial and temporal evolution of magmatic systems beneath the Endeavour Segment, Juan de Fuca Ridge: Tectonic and petrologic constraints. Journal of Geophysical Research: Solid Earth 95 (B12), 19235–19256.

Keller, J.V.A., Pialli, G., 1990. Tectonics of the Island of Elba; a reappraisal. Bollettino della Società Geologica Italiana 109(2), 413–425.

Klein, E.M., 2004. Geochemistry of the Igneous Oceanic Crust, in: Holland, H.D. and Turekian, K.K. (Eds.), Treatise on Geochemistry. Elsevier, Amsterdam, vol. 3, pp. 433–463.

Kligfield, R., Hunziker, J., Dallmayer, R.D., Schamel, S., 1986. Dating of deformation phases using K–Ar and $^{40}Ar/^{39}Ar$ techniques: results from the Northern Apennines. Journal of Structural Geology 8, 781–798.

Lee, J.Y., Marti, K., Severinghaus, J.P., Kawamura, K., Yoo, H.-S., Lee, J.B., Kim, J.S., 2006. A redetermination of the isotopic abundances of atmospheric Ar. Geochimica et Cosmochimica Acta 70, 4507–4512.

Liotta, D., Brogi, A., Meccheri, M., Dini, A., Bianco, C., Ruggieri, G., 2015. Coexistence of low-angle normal and high-angle strike- to oblique-slip faults during Late Miocene mineralization in eastern Elba Island (Italy). Tectonophysics 660, doi: 10.1016/j.tecto.2015.06.025.

Liu, F., Yang, J, Dilek, Y., Xu, Z., Xu, X., Liang, F., Chen, S., 2015. Geochronology and geochemistry of basaltic lavas in the Dongbo and Purang ophiolites of the Yarlung-Zangbo Suture zone: Plume-influenced continental margin-type oceanic lithosphere in southern Tibet. Gondwana Research 27, 701–718.

López-Carmona, A., Abati, J., Pitra, P., Lee, J.K.W., 2014. Retrogressed lawsonite blueschists from the NW Iberian Massif: P-T-t constraints from thermodynamic modelling and $^{40}Ar/^{39}Ar$ geochronology. Contributions to Mineralogy and Petrology 167, 987, doi: 10.1007/s00410-014-0987-5.

Maineri, C., Benvenuti, M., Costagliola, P., Dini, A., Lattanzi, P., Ruggieri, G., Villa, I.M., 2003. Sericitic alteration at the La Crocetta deposit (Elba Island, Italy): interplay between magmatism, tectonics and hydrothermal activity. Mineralium Deposita 38, 67–86.

Martini, I.P., Sagri, M., 1993. Tectono-sedimentary characteristics and the genesis of the recent magmatism of Southern Tuscany and Northern Latium. Per. Mineral. 56, 157–172.

McDonough, W.F., Sun, S.S., 1995. The composition of the Earth. Chemical Geology 120, 223–253.

Molli, G., 2008. Northern Apennine-Corsica orogenic system: an updated overview, in: Siegesmund, S., Fügenschuh, B., Froitzheim, N. (Eds.), Tectonic aspects of the Alpine-Dinaride-Carpathian system. Geological Society, London, Special Publication 298, pp. 413–442.

Musumeci, G., Vaselli, L., 2012. Neogene deformation and granite emplacement in the metamorphic units of northern Apennines (Italy): Insights from mylonitic marbles in the Porto Azzurro pluton contact aureole (Elba Island). Geosphere 8, 470–490, http://doi.org/10.1130/GES00665.1.

Orozbaev, R., Hirajima, T., Bakirov, A., Takasu, A., Maki, K., Yoshida, K., Sakiev K., Bakirov A., Hirata T., Tagirid M., Togonbaeva, A., 2015. Trace element characteristics of clinozoisite pseudomorphs after lawsonite in talc-garnet-chloritoid schists from the Makbal UHP Complex, northern Kyrgyz Tian-Shan. Lithos 226, 98–115, http://doi.org/10.1016/j.lithos.2014.10.008.

Pandeli, E., Puxeddu, M., Ruggieri, G., 2001. The metasiliciclastic-carbonate sequence of the Acquadolce Unit (eastern Elba Island): new petrographic data and palaeogeographic interpretation. Ofioliti 26, 207–218.

Perilli, N., Catanzariti, R., Cascella, A., Nannini, D., 2009. The Calcari di Groppo del Vescovo Formation (Subligurian Units; Northern Apennines, Italy): new dating based on calcareous nannofossils. Atti della Società Toscana di Scienze Naturali 114, 75–83.

Pertusati, P., Raggi, G., Ricci, C.A., Duranti, S., Palmeri, R., 1993. Evoluzione post-collisionale dell'Elba centro-orientale. Memorie della Società Geologica Italiana 49, 297–312.

Plesi G., Bianchi L., Chicchi S., Daniele G., 1993. Le Unità Liguri ed Emiliane della media Val di Taro e la loro evoluzione strutturale. Atti Ticinensi di Scienze della Terra 36, 183–229.

Powell, R., Holland, T.J.B., 1988. An internally consistent dataset with uncertainties and correlations: 3. Applications to geobarometry, worked examples and a computer program. Journal of metamorphic Geology 6, 173–204.

Renne, P.R., Mundil, R., Balco, G., Min, K., Ludwig, K.R., 2010. Joint determination of $^{40}K$ decay constants and $^{40}Ar^{*}/^{40}K$ for the Fish Canyon sanidine standard, and improved accuracy for $^{40}Ar/^{39}Ar$ geochronology. Geochimica et Cosmochimica Acta 74, 5349–5367.

Renne, P.R., Balco, G., Ludwig, K.R., Mundil, R., Min, K., 2011. Response to the comment by WH Schwarz et al. on "Joint determination of $^{40}K$ decay constants and $^{40}Ar^{*}/^{40}K$ for the Fish Canyon sanidine standard, and improved accuracy for $^{40}Ar/^{39}Ar$ geochronology" by PR Renne et al. (2010). Geochimica et Cosmochimica Acta 75, 5097–5100.

Rossetti, F., Faccenna, C., Jolivet, L., Funiciello, R., Tecce, F., Brunet, C. 1999. Syn - versus post-orogenic extension: the case study of Giglio Island (Northern Tyrrhenian Sea, Italy). Tectonophysics 304 (1-2), 71–93.

Rossetti, F., Faccenna, C., Jolivet, L., Goffé, B., Tecce, F., Brunet, C., Funiciello, R., Monié, P., 2001. Structural signature and exhumation P-T-t path of the Gorgona blueschist sequence (Tuscan Archipelago, Italy). Ofioliti 26, 175–186.

Rossetti, F., Faccenna, C., Jolivet, L., Goffé, B., Funiciello, R., 2002. Structural signature and exhumation P-T-t paths of the blueschist units exposed in the interior of the Northern Apennine chain, tectonic implications. Bollettino della Società Geologica Italiana 1, 829–842.

Rossetti, F., Glodny, J., Theye, T., Maggi, M., 2015. Pressure-temperature-deformation-time of the ductile Alpine shearing in Corsica: From orogenic construction to collapse. Lithos 218, 99–116.

Sun, S.S., McDonough, W.S., 1989. Chemical and isotopic systematics of oceanic basalts: implications for mantle composition and processes. Geological Society, London, Special Publications 42, 313–345.

Theye, T., Reinhardt, J., Goffé, B., Jolivet, L., Brunet, C., 1997. Fe- and Mg-carpholite from the Monte Argentario (Italy): first evidence for high-pressure metamorphism of the metasedimentary Verrucano sequence, and significance for P-T path reconstruction. European Journal of Mineralogy 9, 859–873.

Tsujimori, T., Sisson, V.B., Liou, J.G., Harlow, G.E., Sorensen, S.S., 2006. Very-low-temperature record of the subduction process: A review of worldwide lawsonite eclogites. Lithos 92, 609–624.

Ueda, H., Kawamura, M., Niida, K., 2000. Accretion and tectonic erosion processes revealed by the mode of occurrence and geochemistry of greenstones in the Cretaceous accretionary complexes of the Idonnappu Zone, southern central Hokkaido, Japan. Island Arc 9, 237–257.

Vignaroli, G., Faccenna, C., Rossetti, F., Jolivet, L., 2009. Insights from the Apennines metamorphic complexes and their bearing on the kinematics evolution of the orogen, in: Van Hinsbergen, D.J., Edwards, M.A., Govers, R. (Eds), Collision and collapse at the Africa-Arabia-Eurasia subduction zones. Geological Society, London, Special Publications 311, pp. 235–256.

Vitale Brovarone, A., Groppo, C., Hetényi, G., Compagnoni, R., Malavieille, J. 2011. Coexistence of lawsonite-bearing eclogite and blueschist: phase equilibria modelling of Alpine Corsica metabasalts and petrological evolution of subducting slabs. Journal of Metamorphic Geology, 29(5), 583-600.

Vitale Brovarone, A., Herwartz, D., 2013. Timing of HP metamorphism in the Schistes Lustrés of Alpine Corsica: New Lu–Hf garnet and lawsonite ages. Lithos, *172*, 175-191.

Westerman, D.S., Dini, A., Innocenti, F., Rocchi, S., 2004. Rise and fall of a nested Christmas-tree laccolith complex, Elba Island, Italy, in: Breitkreuz, C., Petford, N. (Eds.), Physical Geology of High-Level Magmatic Systems. Geological Society, London, Special Publications 234, pp. 195–213.

White, R.W., Powell, R., Holland, T.J.B., 2007. Progress relating to calculation of partial melting equilibria for metapelites. Journal of Metamorphic Geology 25, 511–527.

Yamato, P., Agard, P., Burov, E., Le Pourhiet, L., Jolivet, L., Tiberi, C., 2007. Burial and exhumation in a subduction wedge: Mutual constraints from thermomechanical modeling and natural P-T-t data (Schistes Lustrés, western Alps). Journal of Geophysical Research: Solid Earth 112(B7), https://doi.org/10.1029/2006JB004441.

Xia, L., Li, X., 2019. Basalt geochemistry as a diagnostic indicator of tectonic setting. Gondwana Research 65, 43–67.

Whitney, D.L., Evans, B.W., 2010. Abbreviations for names of rock-forming minerals. American Mineralogist 95, 185–187.

Zucchi, M., Brogi, A., Liotta, D., Rimondi, V., Ruggieri, G., Montegrossi, G., Caggianelli, A., Dini, A., 2017.Permeability and hydraulic conductivity of faulted micaschist in the eastern Elba Island exhumed geothermal system (Tyrrhenian sea, Italy): insights from Cala Stagnone. Geothermics 70, 125–145.

**Tab. 2** Representative microprobe analyses for metabasite sample RMT3A

| px | | Gln 1** | | Gln 2 cores*** | | Gln 2 rims*** | | Ep | | Czo**** | | Ms**** | | Ph | | Chl | | A |
|---|---|---|---|---|---|---|---|---|---|---|---|---|---|---|---|---|---|---|
| y | ±σ | av(11) | ±σ | av(21) | ±σ | av(24) | ±σ | av(40) | ±σ | av(12) | ±σ | av | ±σ | av | ±σ | av | ±σ | av |
| 2 | 0.54 | 57.78 | 0.66 | 58.26 | 0.24 | 57.94 | 0.37 | 37.26 | 0.71 | 38.60 | 0.66 | 44.63 | 0.15 | 50.04 | 1.25 | 30.22 | 0.30 | 68.39 |
| 3 | 0.07 | 0.15 | 0.08 | 0.11 | 0.08 | 0.15 | 0.10 | 0.08 | 0.07 | 0.14 | 0.10 | 0.14 | 0.05 | 0.04 | 0.01 | 0.03 | 0.03 | 0.02 |
| 4 | 1.14 | 10.01 | 0.55 | 9.70 | 0.63 | 9.23 | 0.72 | 22.39 | 0.78 | 30.36 | 1.66 | 36.87 | 0.44 | 26.34 | 1.11 | 19.16 | 1.44 | 19.96 |
| 3 | 0.27 | 0.02 | 0.02 | 0.01 | 0.01 | 0.01 | 0.01 | 0.02 | 0.02 | 0.03 | 0.03 | 0.01 | 0.01 | 0.02 | 0.02 | 0.11 | 0.07 | 0.01 |
| 2 | 0.73 | 10.47 | 0.35 | 10.42 | 0.52 | 10.98 | 0.56 | 13.68 | 0.69 | 4.83 | 2.24 | 2.06 | 0.26 | 4.74 | 0.30 | 16.64 | 1.93 | 0.22 |
| 0 | 0.05 | 0.18 | 0.06 | 0.18 | 0.04 | 0.18 | 0.05 | 0.23 | 0.16 | 0.11 | 0.05 | 0.01 | 0.01 | 0.02 | 0.02 | 0.28 | 0.05 | 0.01 |
| 0 | 0.51 | 10.97 | 0.34 | 11.29 | 0.37 | 11.36 | 0.40 | 0.00 | 0.00 | 0.00 | 0.00 | 0.13 | 0.13 | 3.46 | 0.25 | 20.72 | 2.19 | 0.12 |
| 2 | 1.07 | 0.91 | 0.33 | 0.78 | 0.27 | 1.11 | 0.58 | 22.61 | 0.52 | 23.62 | 0.64 | 0.31 | 0.17 | 0.04 | 0.03 | 0.21 | 0.42 | 0.38 |
| 5 | 0.55 | 6.80 | 0.27 | 6.47 | 0.28 | 6.23 | 0.45 | 0.01 | 0.02 | 0.06 | 0.04 | 0.54 | 0.29 | 0.08 | 0.01 | 0.11 | 0.35 | 11.63 |
| 1 | 0.16 | 0.03 | 0.03 | 0.04 | 0.03 | 0.06 | 0.07 | 0.01 | 0.02 | 0.08 | 0.14 | 9.50 | 0.25 | 10.39 | 0.13 | 0.05 | 0.13 | 0.05 |
| | | 0.06 | 0.08 | 0.13 | 0.14 | 0.09 | 0.11 | 0.07 | 0.13 | 0.01 | 0.02 | 0.03 | 0.05 | 0.11 | 0.04 | 0.10 | 0.09 | |
| 3 | 0.55 | 97.34 | 0.72 | 97.33 | 0.49 | 97.30 | 0.54 | 96.34 | 1.14 | 97.82 | 0.49 | 98.78 | 0.42 | 99.72 | 0.08 | 89.13 | 1.01 | 100.87 |
| | | | | | | | | | | | | | | | | | | |
| 3 | 0.020 | 7.926 | 0.088 | 7.980 | 0.020 | 7.961 | 0.038 | 2.988 | 0.022 | 2.966 | 0.024 | 6.004 | 0.015 | 6.768 | 0.147 | 5.802 | 0.466 | 2.969 |
| 7 | 0.048 | 1.619 | 0.096 | 1.565 | 0.100 | 1.494 | 0.112 | 2.117 | 0.055 | 2.749 | 0.124 | 5.846 | 0.069 | 4.200 | 0.190 | 4.345 | 0.358 | 1.021 |
| 2 | 0.002 | 0.015 | 0.008 | 0.011 | 0.008 | 0.016 | 0.010 | 0.005 | 0.004 | 0.008 | 0.006 | 0.014 | 0.005 | 0.004 | 0.001 | 0.004 | 0.004 | 0.000 |
| 3 | 0.008 | 0.002 | 0.002 | 0.001 | 0.001 | 0.001 | 0.001 | 0.002 | 0.001 | 0.002 | 0.002 | 0.001 | 0.001 | 0.002 | 0.002 | 0.017 | 0.011 | 0.000 |
| 6 | 0.055 | 0.362 | 0.087 | 0.341 | 0.074 | 0.389 | 0.095 | 0.917 | 0.047 | 0.310 | 0.147 | | | | | 2.204 | 0.261 | 0.008 |
| 3 | 0.051 | 0.839 | 0.073 | 0.835 | 0.044 | 0.856 | 0.062 | | | | | 0.232 | 0.030 | 0.536 | 0.036 | 0.474 | 0.194 | |
| 6 | 0.001 | 0.021 | 0.007 | 0.020 | 0.004 | 0.021 | 0.006 | 0.015 | 0.011 | 0.007 | 0.003 | 0.001 | 0.001 | 0.003 | 0.002 | 0.045 | 0.008 | 0.000 |
| 7 | 0.029 | 2.243 | 0.060 | 2.305 | 0.078 | 2.326 | 0.085 | 0.000 | 0.000 | 0.000 | 0.000 | 0.026 | 0.026 | 0.698 | 0.049 | 5.944 | 0.654 | 0.008 |
| 6 | 0.043 | 0.133 | 0.049 | 0.114 | 0.040 | 0.163 | 0.085 | 1.943 | 0.067 | 1.945 | 0.043 | 0.045 | 0.024 | 0.006 | 0.004 | 0.042 | 0.080 | 0.018 |
| 2 | 0.036 | 1.808 | 0.064 | 1.719 | 0.072 | 1.661 | 0.118 | 0.002 | 0.003 | 0.008 | 0.006 | 0.140 | 0.075 | 0.020 | 0.003 | 0.040 | 0.124 | 0.979 |
| 0 | 0.007 | 0.005 | 0.006 | 0.005 | 0.005 | 0.010 | 0.012 | 0.001 | 0.002 | 0.008 | 0.014 | 1.631 | 0.050 | 1.792 | 0.029 | 0.011 | 0.034 | 0.003 |
| 0 | 0.000 | 14.973 | 0.029 | 14.914 | 0.016 | 14.916 | 0.036 | 7.991 | 0.028 | 8.004 | 0.016 | 13.944 | 0.050 | 14.033 | 0.068 | 18.933 | 0.269 | 5.007 |
| | | 0.026 | 0.028 | 0.056 | 0.059 | 0.039 | 0.044 | 0.018 | 0.032 | 0.001 | 0.004 | 0.012 | 0.020 | 0.047 | 0.017 | 0.057 | 0.054 | |
| 4 | 0.076 | 0.725 | 0.019 | 0.729 | 0.016 | 0.726 | 0.019 | | | | | 0.092 | 0.076 | 0.564 | 0.035 | 0.919 | 0.031 | |

**Tab. 3**: Main mineral assemblages and fabrics in the Rio Marina metabasite

| Metamorphic stage | Main fabric | Main mineral assemblage |
|---|---|---|
| Lawsonite blueschist | Mineral and structural relicts within epidote | Omp/Aeg + Lws + Gln + Chl + Ttn/Rt ± Act |
| Epidote blueschist | Pseudomorph after lawsonite<br>Glaucophane coronas<br>Epidote-rich matrix | Chl + Gln + Act + Omp + Ep + Ttn ± Ph ± Qz |
| Greenschist | Sympectites replacing omphacite<br>Actinote replacing glaucophane | Ep + Act + Ab + Chl + Di + Ttn ± Qz ± Cal |
| Late HT imprint | An replacing Ep in the matrix | An |

HIGHLIGHTS

**The lawsonite-glaucophane blueschists of Elba Island (Italy)**

Caterina Bianco; Gaston Godard; Alison Halton; Andrea Brogi;
Domenico Liotta; Alfredo Caggianelli

- Elba Island metabasites record metamorphic conditions of P ≥ 1.6 GPa and 450–500°C.
- Chlorite-Lawsonite-Glaucophane-Omphacite-Rutile represents the HP-LT metamorphic assemblage.
- The transition from lawsonite-epidote to blueschist facies is dated at 19.8 ± 1.4 Ma and related to collision.
- The Rio Marina metabasites derived from dykes and/or sills with E/T-MORB geochemical affinity.
- The eastern Elba Island units are attributed to the margin of Adria plate.